

Host–Guest Complexation in Wide Bandgap Perovskite Solar Cells

Parnian Ferdowsi,* Gianluca Bravetti, Moritz C. Schmidt, Efrain Ochoa-Martinez, Shanti Bijani, Aurora Rizzo, Silvia Colella, Ullrich Steiner, Bruno Ehrler, Dominik J. Kubicki, and Jovana V. Milić*

Wide-bandgap hybrid halide perovskites are increasingly relevant in the fabrication of tandem solar cells. However, their efficiency and stability during operation are still limited by several factors, among which ion migration at the interface with charge-selective extraction layers is one of the most detrimental ones. Herein, a host–guest complexation strategy is employed to control interfacial ion migration by using dibenzo-21-crown-7 in wide-bandgap hybrid halide perovskites based on methylammonium lead bromide. The capacity of the crown ether is demonstrated that affect the performances and stabilities of MAPbBr₃ solar cells. As a result, power conversion efficiencies of up to 5.9% are achieved with an open circuit voltage as high as 1.5 V, which is accompanied by stability over 300 h at 85 °C under nitrogen atmosphere, as well as more than 300 h at ambient temperature, maintaining ~80% of initial performance. This provides a versatile strategy for wide-bandgap photovoltaic devices.

have been the most widely studied due to their narrow bandgaps between 1.5 and 1.7 eV.^[7–9] However, their poor thermal stability, sensitivity to moisture, and limited reproducibility of the photovoltaic metrics obstruct their commercialization.^[10–16] On the contrary, wide-bandgap perovskite materials, such as methylammonium lead tribromide (MAPbBr₃) with a bandgap of 2.3 eV, can be a promising alternative due to its excellent optoelectronic properties, good charge transport, and higher stability against air and moisture.^[6,7,17,18] MAPbBr₃ can provide a high open-circuit voltage (V_{OC}) value close to 2 V,^[19,20] which makes it suitable for applications in optoelectronics, such as light-emitting diodes, sensors, and tandem solar cells.^[17]

However, these materials also suffer from high nonradiative losses that reduce the V_{OC} and a limited lifetime under operating conditions of elevated temperature, voltage bias, and light that remain unsolved.^[1,21,22]

The lifetime of perovskite solar cells (PSCs) is affected by extrinsic and intrinsic factors. The degradation caused by extrinsic factors is due to the high chemical reactivity of perovskite materials with moisture and oxygen, which can be addressed


1. Introduction

Metal halide perovskites have attracted attention due to their excellent optoelectronic properties, ease of fabrication, and low-cost processing, making them promising candidates for the next generation of photovoltaics.^[1–6] Within the diverse hybrid halide perovskite materials, iodide-based compositions

P. Ferdowsi, G. Bravetti, E. Ochoa-Martinez, U. Steiner, J. V. Milić
Adolphe Merkle Institute
University of Fribourg
1700 Fribourg, Switzerland
E-mail: parnian.ferdowsi@unifr.ch; jovana.milic@unifr.ch

G. Bravetti
Department of Mathematics and Physics “E. De Giorgi”
University of Salento
73100 Lecce, Italy

G. Bravetti, A. Rizzo
CNR NANOTEC – Istituto di Nanotecnologia
73100 Lecce, Italy

 The ORCID identification number(s) for the author(s) of this article can be found under <https://doi.org/10.1002/solr.202300655>.

© 2023 The Authors. Solar RRL published by Wiley-VCH GmbH. This is an open access article under the terms of the Creative Commons Attribution-NonCommercial License, which permits use, distribution and reproduction in any medium, provided the original work is properly cited and is not used for commercial purposes.

DOI: 10.1002/solr.202300655

G. Bravetti, S. Colella
CNR NANOTEC – Istituto di Nanotecnologia, c/o Dipartimento di Chimica
Università di Bari
70125 Bari, Italy

M. C. Schmidt, B. Ehrler
Center for Nanophotonics, FOM Institute AMOLF
1098 XG Amsterdam, Netherlands

S. Bijani
Unidad de Nanotecnología, Centro de Supercomputador y Bioinnovación SCBI
Universidad de Málaga
29590 Campanillas (Málaga), Spain

D. J. Kubicki
Department of Physics
University of Warwick
Coventry CV4 7AL, UK

by encapsulation techniques and compositional engineering of perovskite materials.^[21–26] It has been more challenging to control the intrinsic instability factors, particularly ion migration that is accelerated under operating conditions. While compositional tuning and encapsulation can solve some of these issues,^[21,27,28] ion migration is an inherent characteristic of halide perovskites owing to their mixed conductivities.^[29] This is amplified in the presence of crystal defects, formed mainly at the surface, grain boundaries, and interfaces with the perovskite layer. The defects provide a pathway for ion migration that is amplified during operation. Ion migration can be detrimental to the device's performance and long-term stability, leading to the permanent degradation of PSCs.^[21] It is demonstrated that the organic and halide ions have low activation energy for migration in hybrid halide perovskites, which facilitates their migration through the grain boundaries and defects even at room temperature.^[30] However, halide anion migration was also shown to be partly reversible in the dark, whereas metal and A cation migrations were associated with permanent degradation pathways in perovskite materials and devices.^[31–33] There has been an effort to develop strategies to suppress ion migration, including passivation, controlling crystal growth, and increasing ion migration barriers through substitution.^[30,34–36]

A particularly versatile strategy that has recently been used to control the properties of hybrid halide perovskites relies on host–guest (HG) complexation employing various macrocyclic host (*H*) molecules that can selectively bind and deliver geometrically compatible guest (*G*) species through different noncovalent interactions.^[23,37–41] This approach could control ion migration phenomena, as cations can be effectively bound by *H* moieties using HG complexation. Such HG interactions could affect the perovskite crystal structure and the resulting properties of materials and devices, increasing long-term stability.^[2,42–50] For instance, crown ethers (CEs) are one of the most exploited *H* molecules that have been shown to feature a selectivity to different cations due to a highly electronegative cavity even within hybrid perovskite photovoltaic devices, showing beneficial effects to improving their efficiencies and stabilities.^[2,23,47,48] Despite their potential, there has been limited use of CEs and their HG complexes with metal halide perovskites in solar cells,^[23] with no examples of this strategy being applied to control the properties of wide-bandgap materials or devices to date.

Herein, we demonstrate the utility of dibenzo-21-crown-7 (DB21C7) in wide-bandgap hybrid PSCs based on MAPbBr₃. We show that interfacial modulation yields an open circuit voltage as high as 1.5 V with competitive solar cell performances and enhanced operational stabilities, and provide mechanistic insights into the role of the CE in hybrid PSCs. This represents a promising strategy to control the chemistry of the perovskite precursors and materials, as well as the performances of the resulting devices.

2. Results and Discussion

To assess the effect of HG complexation in wide-bandgap perovskites, we examine three perovskite compositions, namely MAPbBr₃, FA_{0.75}MA_{0.25}PbBr₃, and Cs_{0.05}(FA_{0.75}MA_{0.25})_{0.95}PbBr₃. These materials were prepared through a conventional solution processing method and deposited onto the mesoporous TiO₂ layer by a one-step method using chlorobenzene (CB) as an antisolvent by the procedure detailed in the Experimental Section. For some of the test substrates, DB21C7 solution was deposited on top of the perovskite film as a prospective passivation agent, whereas others were deposited onto the spinning substrate as antisolvent (i.e., mixed into the CB) during film deposition (Figure 1). These approaches are referred to as passivation (*P*) and antisolvent (*AS*) methods, respectively, whereas control samples did not contain any CE moieties. While the CE as a passivation agent (*P*) was applied onto an already formed perovskite film, its use in the *AS* was assumed to affect the perovskite growth, featuring a more pronounced effect on its properties.

It was found that MAPbBr₃ devices exhibit better photovoltaic performances compared to the double- and triple-cation wide-bandgap solar cells. While CE allowed the incorporation of otherwise insoluble CsBr into the composition for wide-bandgap devices (Figure S1–S2, Supporting Information), it did not yield higher photovoltaic performance under these conditions (Table S1, Supporting Information). Therefore, MAPbBr₃ was selected as a model system to assess the effects of DB21C7. The results for other compositions are provided in the Supporting Information (Figure S1–S2 and Table S1, Supporting Information).

The capacity of the DB21C7 to form HG complexes on the surface was evidenced by solid-state nuclear magnetic resonance

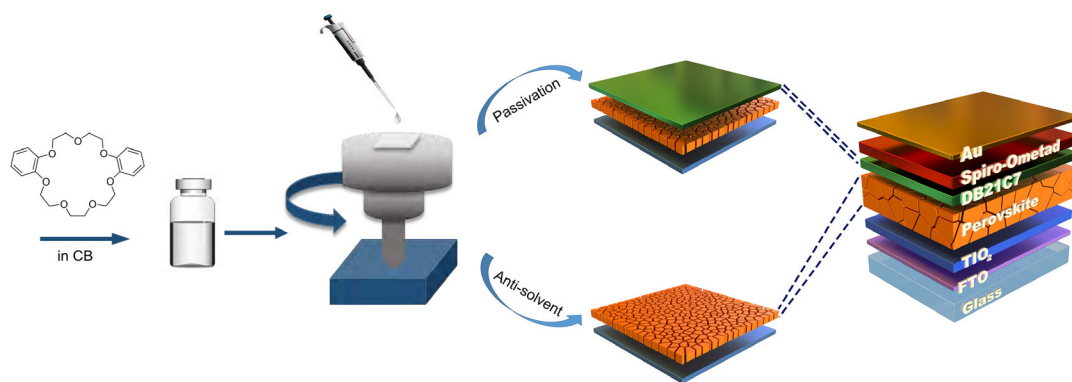


Figure 1. Schematic representation of the MAPbBr₃ film treatment using CE moieties (DB21C7) in CB as either *P* (on top of the perovskite films, i.e., passivation) or *AS* (i.e., antisolvent) for perovskite film casting.

(NMR) spectroscopy (Figure S3, Supporting Information). As complexation of Pb^{2+} and A cations (e.g., FA and Cs cations) has been reported previously,^[49] we recorded magic angle spinning (MAS) solid-state ^{13}C and ^6Li NMR spectra of MAPbBr_3 powders with and without the DB21C7, as well as in the presence of lithium bis(trifluoromethanesulfonyl)imide (LiTFSI), a dopant found to contribute to the instabilities of PSCs.^[31–33] While there were no substantial changes to the ^{13}C signals of CE when combined with MAPbBr_3 and LiTFSI (Figure S3b, Supporting Information), we found that ^6Li NMR is highly sensitive to the speciation of this ion (Figure S3a, Supporting Information). Specifically, the ^6Li NMR spectrum of neat LiTFSI shows a single intense peak at 0.25 ppm (full width at half maximum (FWHM) ≈ 0.1 ppm) corresponding to the solid LiTFSI, and a much smaller and narrower (FWHM: ≈ 0.04 ppm) peak at 0.70 ppm, which can be attributed to trace amounts of hydrated LiTFSI. Upon treatment of MAPbBr_3 with CE and LiTFSI, a new substantially broader (FWHM ≈ 0.6 ppm) peak appears at 0.8 ppm. Since second-order quadrupolar broadening is negligible in ^6Li NMR spectra, we attribute the large linewidth to a distribution of local Li^+ environments corresponding to an interaction with Li^+ . This reveals the capacity for interaction with the Li^+ ions in the sample, which is expected to affect their structural properties and photovoltaic performances.

X-Ray diffraction (XRD) measurements were performed to further investigate the structural properties of perovskite films.

The XRD spectra exhibited typical perovskite peaks at $\sim 15^\circ$ and $\sim 30^\circ$ for all concentrations and preparation methods, corresponding to the (100) and (200) perovskite lattice orientations, respectively (Figure 2a,b). This suggests that DB21C7 does not change the perovskite structure, although evidencing its presence on the surface by X-Ray photoelectron spectroscopy through the corresponding O 1s and C 2s binding energies at 533 and 286 eV, respectively (Figure S4, Supporting Information). However, the concentrations of 5 mg mL^{-1} (AS) and 2.5 mg mL^{-1} (P) were found to increase the intensities of XRD signals, suggesting a possible effect on the crystallinity. The average crystalline size was estimated by resolving the characteristic of (100) and (200) peaks using Scherrer's formula and comparing the FWHM (Table S2, Supporting Information).^[50] The analysis suggests a lower FWHM for 5 mg mL^{-1} (AS) and 1 and 2.5 mg mL^{-1} (P; Table S2, Supporting Information), in accordance with an increase in the crystal sizes.

These effects on the surface morphology were assessed by scanning electron microscopy (SEM). The treated films exhibited a compact and pinhole-free surface coverage with grains smaller than the control samples (Figure 2c,d and Figure S5, Supporting Information). It has been previously suggested that increasing the average grain size can benefit photovoltaic performances.^[51–53] Moreover, ion migration is often assumed to occur across grain boundaries where the CE has been previously suggested to assemble;^[2] hence, it was expected that

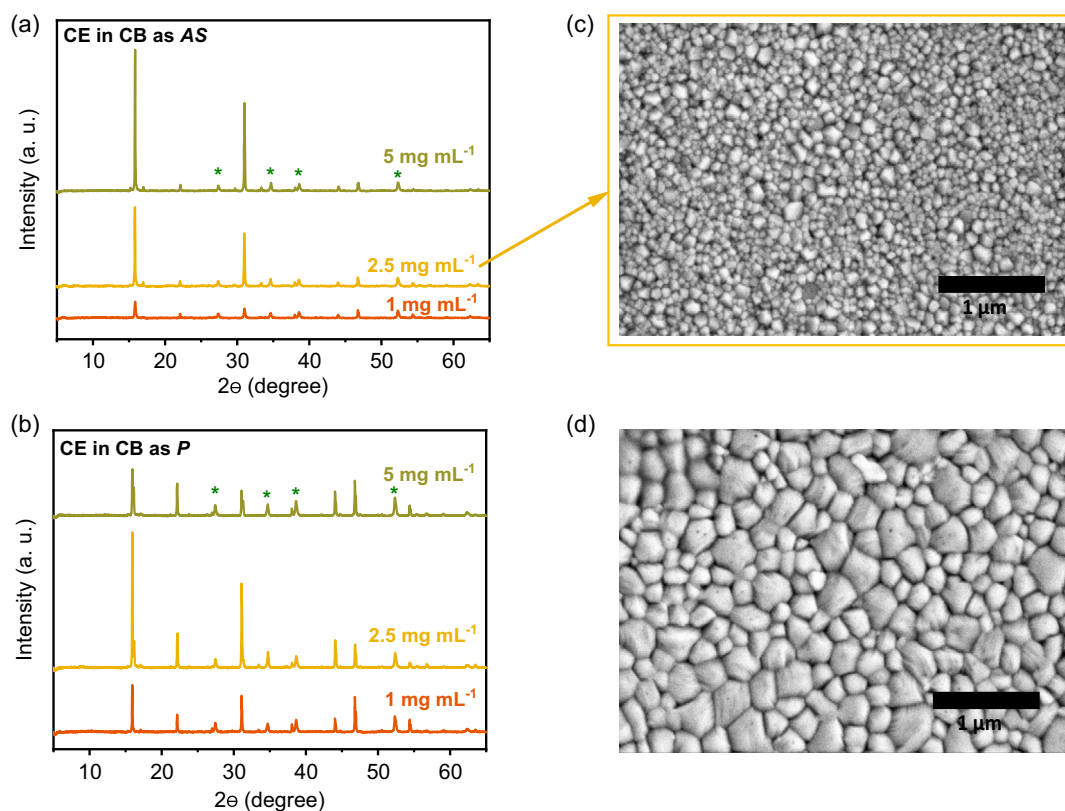


Figure 2. Structural characterization and morphology of the CE-treated MAPbBr_3 films. XRD patterns of samples that are treated by CE as a) AS and b) P agent (the green stars mark the substrate). SEM images of c) treated sample by 2.5 mg mL^{-1} CE as and d) control with regular CB antisolvent treatment.

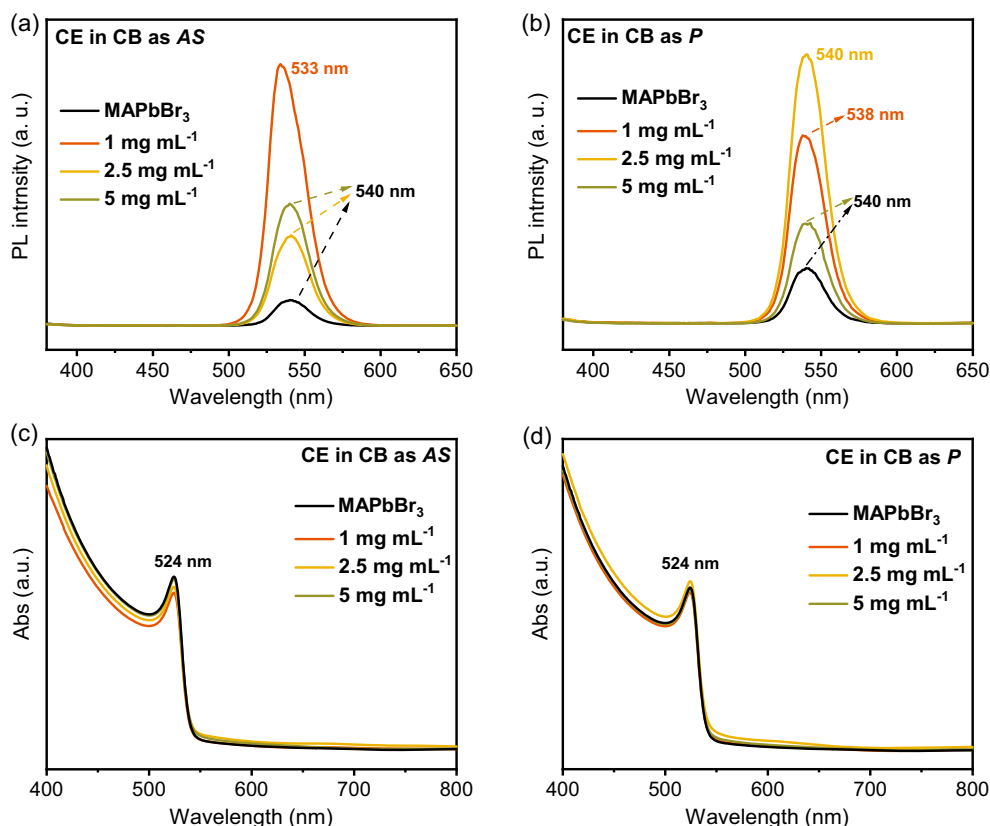


Figure 3. Optical characterization of the MAPbBr₃ casted films treated with CE (in concentrations of 1, 2.5, and 5 mg mL⁻¹). Steady-state PL spectra of treated samples using CE by a) AS and b) *P* method. UV-vis absorption spectra using CE by c) AS and d) *P* method.

the unique capacity of the CE to bind A and metal cations would induce changes in the morphology reflected in the opto(electro) ionic properties and photovoltaic characteristics.

The optoelectronic properties were investigated by steady-state UV-vis absorption and photoluminescence (PL) spectroscopy of thin films and the solar cell models with the fluorine-doped tin oxide (FTO)/compact (c)-TiO₂/mesoporous (mp)-TiO₂/MAPbBr₃/DB21C7 and FTO/c-TiO₂/mp-TiO₂/MAPbBr₃ architectures (Figure 3). The PL spectra of the samples containing 1 or 2.5 mg mL⁻¹ of CE prepared by either AS or *P* method, respectively, display higher PL intensities compared to the others. This is in accordance with the improvements in the crystallinity observed by XRD. However, there is a minor difference in the UV-vis absorption and the corresponding PL spectra, suggesting that the presence of the CE does not substantially affect the film thickness and composition, which are relevant to photovoltaic performances.

To evaluate the effect on the photovoltaic performance when CE is applied at the interface between the perovskite and hole-transport layer (HTL), we prepared cells with and without CE (2.5 mg mL⁻¹) and compared the performances of these devices. The *V*_{OC} and PCE of the solar cells improved from 1.42 ± 0.03 to 1.50 ± 0.01 V and from 4.16 ± 0.53 to 5.21 ± 0.39 on average, respectively (Figure 4a). We noted improvements in all device parameters using CE treatment as AS during film casting. Based on these results, PSCs were fabricated using CE as AS, resulting in a champion cell with a PCE of 5.9%, *V*_{OC} = 1.5 V,

*J*_{SC} = 5.5 mA cm⁻², and fill factor (FF) = 73% (Figure 4b). In contrast, the MAPbBr₃ champion cell without CE achieved a PCE of 5.0%, *V*_{OC} = 1.4 V, *J*_{SC} = 4.9 mA cm⁻², and FF = 71%. The integrated *J*_{SC} obtained by the integration of the incident photon-to-current efficiency (IPCE) spectra for the CE-treated device (2.5 mg mL⁻¹) of 5.1 mA cm⁻² was in good agreement with the *J*_{SC} value obtained from the *J*-*V* characteristics (Figure S6, Supporting Information), excluding any spectral mismatches related to the measurement. The passivated champion device resulted in a PCE of 4.8%, *V*_{OC} = 1.4 V, *J*_{SC} = 5.1 mA cm⁻², and FF = 67%, with a considerable hysteresis (Figure S6, Supporting Information). These results suggest that using CE in CB (at 2.5 mg mL⁻¹ concentration) by AS method is optimal for wide-bandgap perovskites treatment. To further scrutinize the optimized concentration of CE in CB, PSCs were made by AS method using several concentrations (1, 2.5, and 5 mg mL⁻¹), and the resulting photovoltaic metrics confirmed 2.5 mg mL⁻¹ as an optimal concentration in CB (Table S3, Supporting Information).

Having demonstrated the effects of HG complexation on photovoltaic performance, we assessed the long-term thermal stability of devices, including CE-treated (AS) and MAPbBr₃ control samples, in a nitrogen atmosphere at 85 °C upon continuous irradiation (1 sun) for a period of 300 h. A *J*-*V* scan was taken frequently to extract the observed device parameters (Figure 5). CE-treated (2.5 mg mL⁻¹) devices were more stable and demonstrated a lower degradation rate than control devices.

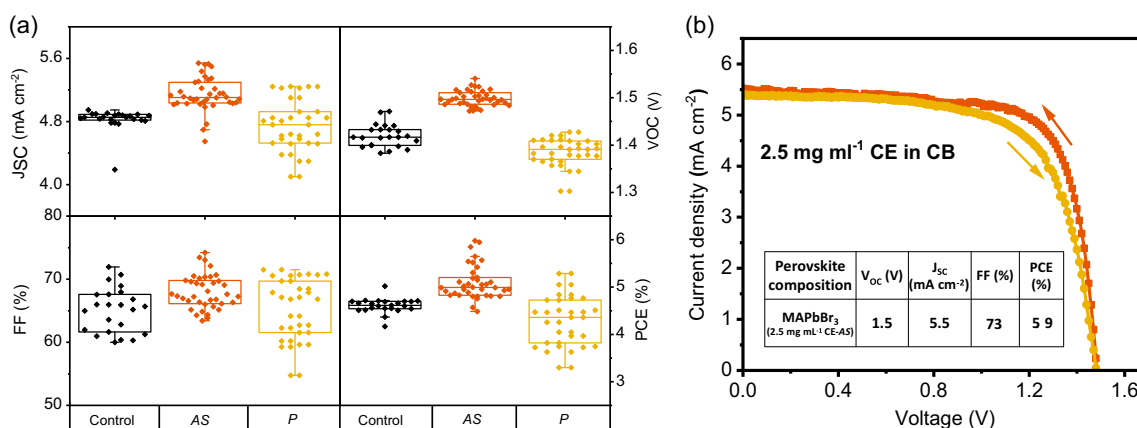


Figure 4. Photovoltaic characteristics. a) Statistical distribution of the photovoltaic parameters for control and CE-treated devices. b) Current–voltage scans for the best-performing device with photovoltaic parameters.

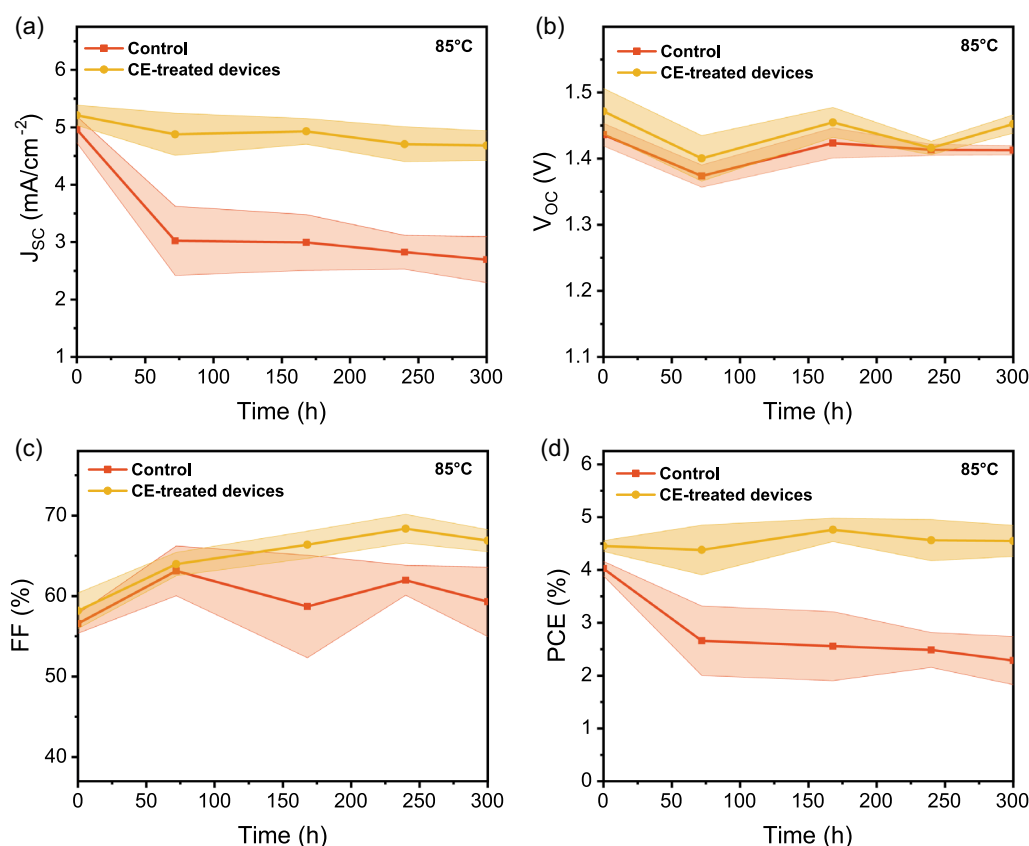


Figure 5. Thermal stability. Evolution of main photovoltaic parameters: a) J_{SC} , b) V_{OC} , c) FF, and d) PCE average of control (red) and CE-treated (yellow) devices. The devices were continuously operated under a nitrogen atmosphere for 300 h at 85 °C in an LED-based solar simulator under 1 sun. Further details are provided in the Methods section. The evolution of key parameters, PCE and V_{OC} , under ambient temperature, is provided in Figure S7 of the Supporting Information.

The thermal stability data highlights CE's significant role through *HG* complexation with the perovskite in long-term stability. The long-term operational stability of the PSCs was further assessed at room temperature by maximum power point tracking of key parameters, PCE and V_{OC} , in a nitrogen atmosphere under continuous LED simulated illumination of 1 sun for

unencapsulated devices. Under these conditions, CE-treated devices maintained over 80% of their PCE after 300 h of continuous measurement, whereas the control devices showed a more significant loss in performance (Figure S7, Supporting Information). The variation of V_{OC} had a similar trend to performance and degradation in both treated and control devices.

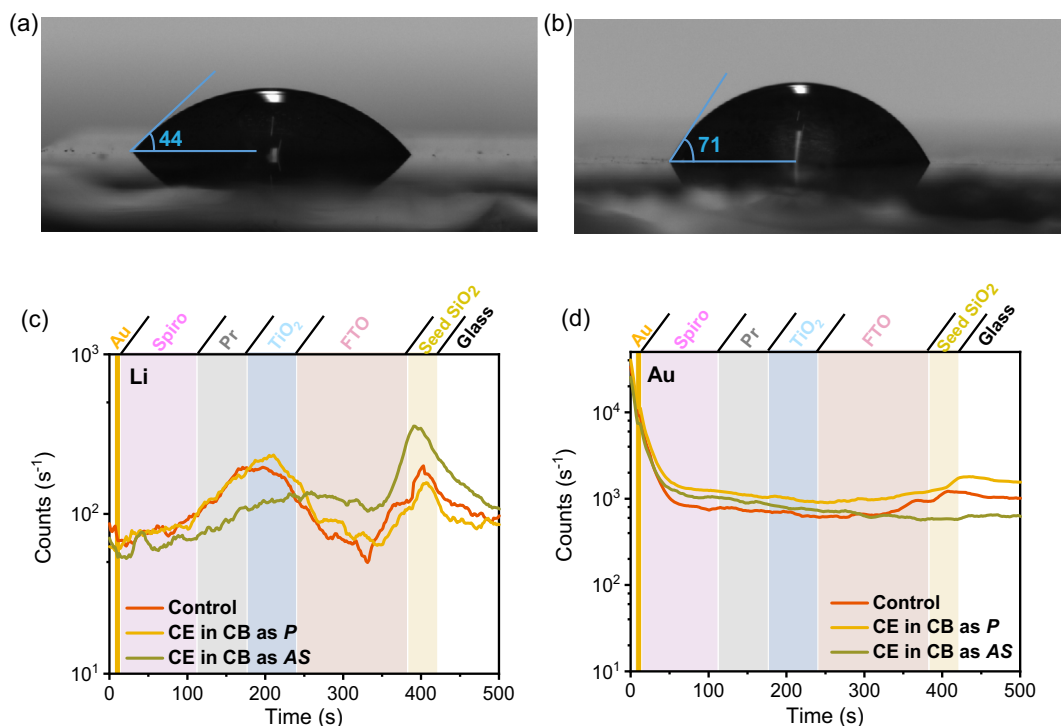


Figure 6. Factors determining the operational stability. a,b) Hydrophobicity comparison by contact angle measurements performed with a water droplet on a) pristine and b) CE-treated perovskite thin films deposited on FTO/c-TiO₂/meso-TiO₂ substrate. c,d) Ion distribution assessment by Li (left) and Au (right) elemental depth profile analysis of MAPbBr₃ by SNMS for control (red line) and treated samples by using AS (green line) and *P* method (yellow line). Further analysis is provided in the Figure S8–S12 (Supporting Information).

Enhanced thermal stability and low degradation rate of CE-treated devices under operating conditions were attributed to the CE interactions at the interface with the hole-transport material that could be related to the changes in hydrophobicity and the effect on ion migration.

The changes in hydrophobicity were assessed by measuring the contact angle of a water droplet on top of the perovskite film on FTO/c-TiO₂/mesoporous-TiO₂ substrates with and without CE. This angle increased from 44° to 71° after depositing CE solution onto the spinning substrate (as AS) during perovskite film preparation, which suggests that CE can contribute to an increase in hydrophobicity (Figure 6). A more hydrophobic layer is relevant to the improvements in the contacts with the HTL and potentially in blocking water ingress.^[54,55]

To gain additional insight into the impact of the HG complexation on the bulk device characteristics and their ion migration, we carried out impedance spectroscopy in the frequency range from 0.5 Hz to 500 kHz at temperatures between 210 and 330 K (as detailed in the Experimental Section and the Supporting Information). We fitted the impedance spectra with the equivalent circuit (Figure S8, Supporting Information) consisting of the series resistance (R_s) and two elements with a resistance parallel to a constant phase element ($R_{p1}||Q_{p1}$ and $R_{p2}||Q_{p1}$). We extracted the parallel resistances corresponding to the high-frequency (R_{p1}) and low-frequency (R_{p2}) signatures of the impedance (Figure S9, Supporting Information) and compared them for control and treated devices. Both devices show a similar evolution of R_{p1} and R_{p2} as a function of

temperature. This comparable behavior is likely in accordance with the treatment not affecting bulk materials' properties. We thereby further performed secondary neutral mass spectroscopy (SNMS) measurements to assess CE's role in interfacial ion migration. SNMS profiles of control and CE-treated devices through AS and *P* show the distribution of constituent elements (Figure S10–S12, Supporting Information), namely, Li, C, O, Si, Ti, Br, Sn, Au, and Pb, which are ordered in terms of their atomic weight. The analysis of the control sample (Figure S10, Supporting Information and Figure 6c,d) demonstrates that the initially high concentration of Au is followed by a decrease in the Au signal and an increase in the C signal, which could be mainly attributed to the hole-transport material (Spiro-OMeTAD). Whereas control and CE-treated devices (*P*) show similar spectral characteristics, CE devices treated by the AS method display a distinct behavior. This is in accordance with the differences in their morphologies evidenced by XRD and SEM analysis. Specifically, traces of Li are found in both perovskite and TiO₂ layers for control and CE-treated samples by the *P* method. In contrast, lower diffusion of Li ions was observed in the perovskite layer for CE-treated by AS method (Figure 6c and S10a, Supporting Information), evidencing the effect of HG complexation on the ion distribution at the interface that corroborates beneficial changes in the material and device characteristics. The versatility of this strategy provides opportunities for extending its scope across perovskite compositions and device architectures toward further advancement and optimization in the future.

3. Conclusion

In summary, we demonstrate the role of *HG* complexation by a crown ether (dibenzo-21-crown-[7], DB21C7) on wide-bandgap perovskite devices and reveal the mechanistic origins of the effects. The presence of DB21C7 does not substantially affect the structural or optoelectronic properties of the perovskite material, yet it alters the morphology while increasing the hydrophobicity of the MAPbBr₃. Moreover, although ion migration through the bulk of the perovskite remains comparable to the untreated devices, we find a lower diffusion of ions across the interface (especially Au and Li) for the CE-treated sample, suggesting an interfacial effect of *HG* complexation on the ion migration. As a result, we obtained wide-bandgap perovskite with improved photovoltaic performance (PCE of 5.9% and V_{OC} of 1.5 V) compared to the nontreated perovskite devices (PCE of 5.0% and V_{OC} of 1.4 V). While these photovoltaic characteristics are competitive compared to some of the other MAPbBr₃ n-i-p perovskite device architectures reported to date,^[56] they can be further improved. For instance, the record-performing state-of-the-art wide-bandgap MAPbBr₃ PSCs of p-i-n architectures feature power conversion efficiencies that exceed 10% with open circuit voltages beyond 1.6 V, which was achieved using e-beam processing, vacuum annealing, and atomic layer deposition.^[4] However, the corresponding operational stabilities remain to be assessed.^[4,56] In this regard, the versatile *HG* complexation provides an opportunity for further optimization. This is particularly due to the desirable increase in the V_{OC} for tandem solar cells and other optoelectronic devices that require a wide bandgap. Moreover, this is accompanied by high stability at elevated temperatures of 85 °C in a nitrogen atmosphere and enhanced operational stability during irradiation. The *HG* complexation thereby offers a promising strategy to extend the scope and better control ion migration, improving operational stability without compromising the performances of wide-bandgap PSCs.

4. Experimental Section

Materials: The materials used were commercially available. All solvents and chemicals were used without further purification.

Perovskite solution preparation relied on the molar ratios for MABr: PbBr₂, FABr: PbBr₂, CsBr: PbBr₂, and CsBr: DB21C7 were fixed at 1:1, 1:1.09, 1:1 and 1:1, respectively. The solutions were prepared from precursor solutions in the mixture of anhydrous *N,N*-dimethylformamide (DMF), and dimethylsulfoxide (DMSO) 4:1 (v:v) to obtain the final perovskite solutions (1.3 M). Double cation perovskite solution was obtained by mixing 75:25 ratios of MA: FA solutions. Similarly, a triple cation solution was prepared using DB21C7 to solubilize 5% of CsBr. MAPbBr₃ precursor solution was prepared from a solution containing MABr and PbBr₂ (1.5 M) in anhydrous DMF: DMSO 4:1 (v:v). The PbBr₂ solution was added to MABr powder with a 1:1 molar ratio to obtain the final perovskite solution (1.3 M). CE precursor solution was prepared by dissolving 1, 2.5, or 5 mg DB21C7 (as indicated in the manuscript discussion and figure captions) in 1 mL CB. The prepared solutions were spin-coated dynamically onto a rotating substrate at 4000 rpm for 30 s on top of the perovskite layer or deposited onto the spinning substrate as antisolvent approximately 10 s before the end of the program during perovskite film deposition.

Solar Cell Device Fabrication: FTO preetched substrates (Sigma-Aldrich, TEC-7) were cleaned by ultrasonication in 2% Hellmanex water solution, isopropyl alcohol, and ethanol, respectively. All substrates were further plasma washed for 3 min in a Zepto plasma system from Diener

Electronic in an oxygen atmosphere at a pressure of around 0.4–0.6 mbar and using 20–30 W of plasma power. A compact TiO₂ layer was deposited on FTO through spray pyrolysis, using oxygen as a carrier gas, at 450 °C from a precursor of titanium diisopropoxide bis(acetylacetonate) stock solution (75 wt% in isopropanol) and acetylacetone in anhydrous ethanol. *In the next step*, a mesoporous TiO₂ layer was deposited by spin coating using a 30 nm particle paste (Dyesol 30 NR-D) diluted in ethanol (100 mg mL⁻¹). After that, the substrates were sintered with a ramped temperature profile, keeping the temperature at 125, 225, 375, 450, and 25 °C for 5, 5, 5, and 30 min, respectively, with 5, 15, 5, and 5 min ramp duration between each temperature. The mesoporous TiO₂ film was further Li-doped by spin coating of Li-TFSI (Aldrich) solution in acetonitrile (10 mg mL⁻¹). The substrates were then transferred to deposit the perovskite films in a nitrogen atmosphere glove box.^[57] The perovskite layer was deposited from solution by spin-coating at 3000 rpm and acceleration of 2000 rpm s⁻¹ for 22.5 s. About 10 s before the end of the program, 100 µL of CB or CE solution in CB was deposited onto the spinning substrate. The film immediately changed to a yellow appearance. After spin coating, the films were annealed at 100 °C for 45 min in a nitrogen-filled glove box. The substrates were cooled down for a couple of minutes, and CE solution was deposited on a rotating substrate at 4000 rpm for 30 s for those samples using CB as an antisolvent, followed by annealing the substrates at 80 °C for 10 min. Thereafter, HTM was deposited by using 2,2',7,7'-tetrakis-(*N*, *N*-di-4-methoxyphenylamino)-9,9'-spirobifluorene (Spiro-OMeTAD, Lumtec) solution (70 mM in CB) spin-coated at 4000 rpm for 20 s. Spiro-OMeTAD was doped with Li-TFSI and 4-*tert*-Butylpyridine (TBP, Sigma-Aldrich). The molar ratio was 0.5 and 3.3 for Li-TFSI and TBP, respectively. Finally, 80 nm of gold top electrode was thermally evaporated under a high vacuum (at 2×10^{-6} Torr).

Photovoltaic devices were tested under simulated solar irradiation (100 mW cm⁻², AM 1.5G) using a solar simulator from ABET Technologies (Model Sun 2000) with a xenon arc lamp, and the solar cell response was recorded using an EmStat3 Blue potentiostat from PalmSens. The light intensity was calibrated using a silicon reference cell from ReRa Solutions (KG5 filtered). Current–voltage curves were measured with a scan rate of 20 mV s⁻¹. The device area was 0.16 cm² (0.4 cm × 0.4 cm). The cells were masked with a black metal mask (0.10 cm²), which determines the active area and reduces the influence of the scattered light.

UV-vis measurements were performed using a Shimadzu UV-2401PC spectrophotometer.

PL measurements on perovskite films were performed using a Horiba Fluorolog FL 3-22 (short-arc xenon discharge lamps) spectrometer.

SEM images were carried out with a Scios 2 DualBeam FIB-SEM from FEI operated at an acceleration voltage of 5 kV. Optical microscopy was done using a ZEISS Axio Scope.A1 microscope.

⁶Li, ¹³C, and ¹H-¹³C cross-polarization (CP) MAS NMR spectra were recorded on a Bruker Avance Neo 11.7 T spectrometer equipped with a 3.2 mm CPMAS probe and referenced to the ¹³C CH₂ peak of adamantane (38.48 ppm). 86 kHz ¹H decoupling was used. Recycle delays of 260 s (⁶Li), 10–0.5 s (¹³C, neat LiTFSI), 10 s (¹³C, neat MAPbI₃), 7 s (¹H-¹³C CP, neat CE), and 15 s (¹H-¹³C CP, MAPbBr₃ + CE + LiTFSI) were used. The rotors were spun using dry nitrogen.

XRD measurements of thin films were performed on a Rigaku Ultima-IV diffractometer using Cu K_α radiation in a Bragg–Brentano configuration.

X-Ray photoelectron spectroscopy measurements were carried out on an Axis Supra (Kratos Analytical) using the monochromated Ka X-Ray line of an aluminum anode. The pass energy was set to 20 eV with a step size of 0.1 eV. The samples were electrically grounded to limit charging effects.

The impedance spectra were recorded using a Zurich Instruments MFIA. During the measurements, the devices were located in a Janis VPF-100 liquid nitrogen cryostat at a pressure below 5×10^{-6} mbar. The temperature was controlled with a Lakeshore 335 temperature controller and was swept from 210 to 330 K in steps of 6 K. At each temperature step; the temperature was stabilized for 10 min. The impedance spectra were recorded in a frequency range from 0.5 Hz to 500 kHz with an AC voltage amplitude of 20 mV. We carry out impedance spectroscopy in the frequency range from 0.5 Hz to 500 kHz at temperatures between 210

and 330 K. The impedance spectra were fitted with the equivalent circuit (Figure S8, Supporting Information), consisting of the series resistance (R_s) and two elements with a resistance parallel to a constant phase element ($R_{p1}||Q_{p1}$ and $R_{p2}||Q_{p1}$). Example fits of a reference device at 216.0, 270.0, and 330.0 K are shown in Figure S8 (Supporting Information). The parallel resistances corresponding to the high-frequency (R_{p1}) and low-frequency (R_{p2}) signatures of the impedance were then extracted. The reference and the target devices show a similar evolution of R_{p1} and R_{p2} as a function of temperature. The high-frequency resistance R_{p1} decreases with increasing temperature. For R_{p2} , we can identify two thermally activated regions where the resistance decreases between 210 and 260 K and 280 and 330 K. A broad distribution of values across samples did not permit a more quantitative comparison.

The IPCE spectra were measured in an Arkeo system from CICC Research. The excitation was provided with a 300 W Xenon lamp. The measurement is performed in the range between 300 and 900 nm with a step size of 10 nm, no supplemental illumination or bias has been used during the measurement. The spot for the measurement was approximately 3 mm wide.

The operational stability of the cells was measured with Litos, advanced solar cell and LED lifetime stability measurement system under a white light-emitting diode illumination (1 sun). It was performed under a continuous nitrogen flow at room temperature or 85 °C (as indicated in the manuscript and figure captions) for unencapsulated devices. The light intensity was adjusted using the current matching of a Si reference diode.

SNMS depth profiles of the samples were recorded by an SNMS equipment type INA-X (SPECS, GmbH, Berlin, Germany). The samples were analyzed in high-frequency bombardment mode using a Kr plasma. The radio frequency discharge conditions were 300 kHz and 80% duty cycle. The Kr pressure was about 2.3×10^{-3} mbar. The Kr ions were extracted from the plasma using high-frequency negative bias at 1000 V for the sample sputtering to achieve high-depth resolution. Samples were mounted on a Cu sample holder with a Ta mask pressing the sample to the support. The sputtered sample area was given by the circular Ta mask opening of 3 mm, coinciding almost with the full area of the evaporated pixel. All experiments were run with a 7.5 mm Mo aperture as the entrance to the plasma chamber with a distance between this aperture and the surface sample of 2.9 mm.

Contact angle measurements were performed using the contact angle system OCA 15Pro for nontreated and CE-treated samples. Small drops of water–2 μ L were released on the surface of the perovskite film on FTO/c-TiO₂/mesoporous-TiO₂ substrates without/with CE treatment. High-resolution images of water droplets on the surface of the samples were collected using IDS UI-222xSE-M R3 camera and SCA20 software.

Supporting Information

Supporting Information is available from the Wiley Online Library or from the author.

Acknowledgements

P.F., U.S., and J.V.M. are grateful to the Adolphe Merkle Foundation and DFG-SPP funding. J.V.M. acknowledges the support of Swiss National Science Foundation PRIMA grant no. 193174. The work of M.C.S. and B.E. was carried out at the research institute AMOLF as part of NWO and is part of a project that has received funding from the European Research Council (ERC) under the European Union's Horizon 2020 research and innovation program (grant agreement no. 947221). A.R. acknowledges the projects "Mission Innovation, IEMAP" founded by Ministero della Transizione Ecologica, MiTE (CUP B82C21001820001) and "New concepts, materials and technologies for the building integration of photovoltaics in a scenario of diffuse generation" (CANVAS) founded by Ministero della Transizione Ecologica (MiTe). S.C. acknowledges project Ricerca@Cnr PHOTOCAT (CUP B93C21000060006). The

authors appreciate Dr. Mounir Mensi (EPFL) for his help with XPS measurements.

Conflict of Interest

The authors declare no conflict of interest.

Author Contributions

The manuscript was written by P.F. with the support of all authors. The study was conceptualized by P.F. and J.V.M., who directed the project. P.F. performed material and device fabrication and characterization with the support of E.O.-M. and G.B., who were jointly supervised by J.V.M., A.R., and S.C. Furthermore, M.C.S. and B.E. performed the transient ion drift measurements and analysis. U.S. was involved in the discussions and the supervision of P.F., whereas S.B. performed the SNMS measurements. All authors were involved in the discussions and approved the final manuscript version. D.J.K. performed NMR analysis.

Data Availability Statement

Data presented here can be accessed at <https://doi.org/10.5281/zenodo.10184416>, and it is available under the license CC-BY-4.0 (Creative Commons Attribution-ShareAlike 4.0 International).

Keywords

host–guest complexation, hybrid perovskites, wide-bandgap semiconductors

Received: August 24, 2023

Revised: September 29, 2023

Published online:

- [1] R. Chen, Y. Hui, B. Wu, Y. Wang, X. Huang, Z. Xu, P. Ruan, W. Zhang, F. Cheng, W. Zhang, J. Yin, J. Li, N. Zheng, *J. Mater. Chem. A* **2020**, *8*, 9597.
- [2] T.-S. Su, F. T. Eickemeyer, M. A. Hope, F. Jahanbakhshi, M. Mladenović, J. Li, Z. Zhou, A. Mishra, J.-H. Yum, D. Ren, A. Krishna, O. Ouellette, T.-C. Wei, H. Zhou, H.-H. Huang, M. D. Mensi, K. Sivula, S. M. Zakeeruddin, J. V. Milić, A. Hagfeldt, U. Rothlisberger, L. Emsley, H. Zhang, M. Grätzel, *J. Am. Chem. Soc.* **2020**, *142*, 19980.
- [3] M. Saliba, T. Matsui, J.-Y. Seo, K. Domanski, J.-P. Correa-Baena, M. K. Nazeeruddin, S. M. Zakeeruddin, W. Tress, A. Abate, A. Hagfeldt, M. Grätzel, *Energy Environ. Sci.* **2016**, *9*, 1989.
- [4] X. Hu, X. Jiang, X. Xing, L. Nian, X. Liu, R. Huang, K. Wang, H. Yip, G. Zhou, *Solar RRL* **2018**, *2*, 1800083.
- [5] P. Ferdowsi, E. Ochoa-Martinez, U. Steiner, M. Saliba, *Chem. Mater.* **2021**, *33*, 3971.
- [6] P. Ferdowsi, E. Ochoa-Martinez, S. S. Alonso, U. Steiner, M. Saliba, *Sci. Rep.* **2020**, *10*, 22260.
- [7] Q. Chen, N. De Marco, Y. (Michael) Yang, T.-B. Song, C.-C. Chen, H. Zhao, Z. Hong, H. Zhou, Y. Yang, *Nano Today* **2015**, *10*, 355.
- [8] Y. Zhao, H. Tan, H. Yuan, Z. Yang, J. Z. Fan, J. Kim, O. Voznyy, X. Gong, L. N. Quan, C. S. Tan, J. Hofkens, D. Yu, Q. Zhao, E. H. Sargent, *Nat. Commun.* **2018**, *9*, 1607.
- [9] F. Liu, Y. Zhang, C. Ding, T. Toyoda, Y. Ogomi, T. S. Ripolles, S. Hayase, T. Minemoto, K. Yoshino, S. Dai, Q. Shen, *J. Phys. Chem. Lett.* **2018**, *9*, 294.

- [10] M. Kulbak, S. Gupta, N. Kedem, I. Levine, T. Bendikov, G. Hodes, D. Cahen, *J. Phys. Chem. Lett.* **2016**, 7, 167.
- [11] D. Prochowicz, P. Yadav, M. Saliba, D. J. Kubicki, M. Mahdi, S. M. Zakeeruddin, J. Lewi, L. Emsley, M. Grätzel, *Nano Energy* **2018**, 49, 523.
- [12] C. Yi, J. Luo, S. Meloni, A. Boziki, N. Astani, C. Grätzel, S. Zakeeruddin, U. Rothlisberger, M. Graetzel, *Energy Environ. Sci.* **2015**, 9, 656.
- [13] S. D. Stranks, G. E. Eperon, G. Grancini, C. Menelaou, M. J. P. Alcocer, T. Leijtens, L. M. Herz, A. Petrozza, H. J. Snaith, *Science* **2013**, 342, 341.
- [14] Y. Han, S. Meyer, Y. Dkhissi, K. Weber, J. M. Pringle, U. Bach, L. Spiccia, Y.-B. Cheng, *J. Mater. Chem. A* **2015**, 3, 8139.
- [15] J. Yang, B. D. Siempelkamp, D. Liu, T. L. Kelly, *ACS Nano* **2015**, 9, 1955.
- [16] N. Kedem, T. M. Brenner, M. Kulbak, N. Schaefer, S. Levchenko, I. Levine, D. Abou-Ras, G. Hodes, D. Cahen, *J. Phys. Chem. Lett.* **2015**, 6, 2469.
- [17] C. A. López, M. V. Martínez-Huerta, M. C. Alvarez-Galván, P. Kayser, P. Gant, A. Castellanos-Gomez, M. T. Fernández-Díaz, F. Fauth, J. A. Alonso, *Inorg. Chem.* **2017**, 56, 14214.
- [18] L. McGovern, M. H. Futscher, L. A. Muscarella, B. Ehrler, *J. Phys. Chem. Lett.* **2020**, 11, 7127.
- [19] R. D. J. Oliver, P. Caprioglio, F. Peña-Camargo, L. R. V. Buizza, F. Zu, A. J. Ramadan, S. G. Motti, S. Mahesh, M. M. McCarthy, J. H. Warby, Y.-H. Lin, N. Koch, S. Albrecht, L. M. Herz, M. B. Johnston, D. Neher, M. Stollerfoht, H. J. Snaith, *Energy Environ. Sci.* **2022**, 15, 714.
- [20] C.-G. Wu, C.-H. Chiang, S. H. Chang, *Nanoscale* **2016**, 8, 4077.
- [21] L. Meng, J. You, Y. Yang, *Nat. Commun.* **2018**, 9, 5265.
- [22] J.-W. Lee, S.-G. Kim, J.-M. Yang, Y. Yang, N.-G. Park, *APL Mater.* **2019**, 7, 41111.
- [23] P. Ferdowsi, U. Steiner, J. V. Milić, *J. Phys. Mater.* **2021**, 4, 42011.
- [24] Q. Dong, F. Liu, M. K. Wong, H. W. Tam, A. B. Djurišić, A. Ng, C. Surya, W. K. Chan, A. M. C. Ng, *ChemSusChem* **2016**, 9, 2597.
- [25] S. Seo, S. Jeong, C. Bae, N.-G. Park, H. Shin, *Adv. Mater.* **2018**, 30, 1801010.
- [26] J.-W. Lee, D.-H. Kim, H.-S. Kim, S.-W. Seo, S. M. Cho, N.-G. Park, *Adv. Energy Mater.* **2015**, 5, 1501310.
- [27] N. Arora, M. I. Dar, A. Hinderhofer, N. Pellet, F. Schreiber, S. M. Zakeeruddin, M. Grätzel, *Science* **2017**, 358, 768.
- [28] P. Wang, X. Zhang, Y. Zhou, Q. Jiang, Q. Ye, Z. Chu, X. Li, X. Yang, Z. Yin, J. You, *Nat. Commun.* **2018**, 9, 2225.
- [29] M. H. Futscher, J. V. Milić, *Front. Energy Res.* **2021**, 9, 1.
- [30] D. Wei, F. Ma, R. Wang, S. Dou, P. Cui, H. Huang, J. Ji, E. Jia, X. Jia, S. Sajid, A. M. Elseman, L. Chu, Y. Li, B. Jiang, J. Qiao, Y. Yuan, M. Li, *Adv. Mater.* **2018**, 30, 1707583.
- [31] K. Domanski, E. A. Alharbi, A. Hagfeldt, M. Grätzel, W. Tress, *Nat. Energy* **2018**, 3, 61.
- [32] K. Domanski, B. Roose, T. Matsui, M. Saliba, S.-H. Turren-Cruz, J.-P. Correa-Baena, C. R. Carmona, G. Richardson, J. M. Foster, F. De Angelis, J. M. Ball, A. Petrozza, N. Mine, M. K. Nazeeruddin, W. Tress, M. Grätzel, U. Steiner, A. Hagfeldt, A. Abate, *Energy Environ. Sci.* **2017**, 10, 604.
- [33] K. Domanski, J.-P. Correa-Baena, N. Mine, M. K. Nazeeruddin, A. Abate, M. Saliba, W. Tress, A. Hagfeldt, M. Grätzel, *ACS Nano* **2016**, 10, 6306.
- [34] Y. Shao, Z. Xiao, C. Bi, Y. Yuan, J. Huang, *Nat. Commun.* **2014**, 5, 5784.
- [35] D. Wei, J. Ji, D. Song, M. Li, P. Cui, Y. Li, J. M. Mbengue, W. Zhou, Z. Ning, N.-G. Park, *J. Mater. Chem. A* **2017**, 5, 1406.
- [36] W. Ke, C. Xiao, C. Wang, B. Saparov, H.-S. Duan, D. Zhao, Z. Xiao, P. Schulz, S. P. Harvey, W. Liao, W. Meng, Y. Yu, A. J. Cimaroli, C.-S. Jiang, K. Zhu, M. Al-Jassim, G. Fang, D. B. Mitzi, Y. Yan, *Adv. Mater.* **2016**, 28, 5214.
- [37] G. Yu, X. Chen, *Theranostics* **2019**, 9, 3041.
- [38] T. Aida, E. W. Meijer, S. I. Stupp, *Science* **2012**, 335, 813.
- [39] J.-M. Lehn, *Chem. Soc. Rev.* **2017**, 46, 2378.
- [40] L. Yang, X. Tan, Z. Wang, X. Zhang, *Chem. Rev.* **2015**, 115, 7196.
- [41] D. J. Cram, S. Karbach, H. E. Kim, C. B. Knobler, E. F. Maverick, J. L. Ericson, R. C. Helgeson, *J. Am. Chem. Soc.* **1988**, 110, 2229.
- [42] S. Huang, T. Zhang, C. Jiang, R. Qi, C. Luo, Y. Chen, H. Lin, J. Travas-sejdic, H. Peng, *ChemNanoMat* **2019**, 5, 1311.
- [43] J. Li, T. Jiu, S. Chen, L. Liu, Q. Yao, F. Bi, C. Zhao, Z. Wang, M. Zhao, G. Zhang, Y. Xue, F. Lu, Y. Li, *Nano Lett.* **2018**, 18, 6941.
- [44] P. Vashishtha, S. A. Veldhuis, S. S. H. Dintakurti, N. L. Kelly, B. E. Griffith, A. A. M. Brown, M. S. Ansari, A. Bruno, N. Mathews, Y. Fang, T. White, S. G. Mhaisalkar, J. V. Hanna, *J. Mater. Chem. C* **2020**, 8, 11805.
- [45] Y. Takashima, A. Harada, *J. Incl. Phenom. Macrocycl. Chem.* **2017**, 87, 313.
- [46] J. Teyssandier, S. De Feyter, K. S. Mali, *Chem. Commun.* **2016**, 52, 11465.
- [47] S. A. Veldhuis, Y. F. Ng, R. Ahmad, A. Bruno, N. F. Jamaludin, B. Damodaran, N. Mathews, S. G. Mhaisalkar, *ACS Energy Lett.* **2018**, 3, 526.
- [48] R. Chen, Y. Wu, Y. Wang, R. Xu, R. He, Y. Fan, X. Huang, J. Yin, B. Wu, J. Li, N. Zheng, *Adv. Funct. Mater.* **2020**, 2020, 2008760.
- [49] H. Zhang, F. T. Eickemeyer, Z. Zhou, M. Mladenović, F. Jahanbakhshi, L. Merten, A. Hinderhofer, M. A. Hope, O. Ouellette, A. Mishra, P. Ahlawat, D. Ren, T.-S. Su, A. Krishna, Z. Wang, Z. Dong, J. Guo, S. M. Zakeeruddin, F. Schreiber, A. Hagfeldt, L. Emsley, U. Rothlisberger, J. V. Milić, M. Grätzel, *Nat. Commun.* **2021**, 12, 3383.
- [50] E. S. Parrott, J. B. Patel, A.-A. Haghighirad, H. J. Snaith, M. B. Johnston, L. M. Herz, *Nanoscale* **2019**, 11, 14276.
- [51] G. W. P. Adhyaksa, S. Brittman, H. Ąboliņš, A. Lof, X. Li, J. D. Keelor, Y. Luo, T. Duevski, R. M. A. Heeren, S. R. Ellis, D. P. Fenning, E. C. Garnett, *Adv. Mater.* **2018**, 30, 1804792.
- [52] B. Hwang, Y. Park, J.-S. Lee, *J. Mater. Chem. C* **2021**, 9, 110.
- [53] O. Shargaieva, F. Lang, J. Rappich, T. Ditttrich, M. Klaus, M. Meixner, C. Genzel, N. H. Nickel, *ACS Appl. Mater. Interfaces* **2017**, 9, 38428.
- [54] X. He, M. Wang, F. Cao, W. Tian, L. Li, *J. Mater. Sci. Technol.* **2022**, 124, 243.
- [55] Y. Li, J. V. Milić, A. Ummadisingu, J.-Y. Seo, J.-H. Im, H.-S. Kim, Y. Liu, M. I. Dar, S. M. Zakeeruddin, P. Wang, A. Hagfeldt, M. Grätzel, *Nano Lett.* **2019**, 19, 150.
- [56] C. Aranda, A. Guerrero, J. Bisquert, *ACS Energy Lett.* **2019**, 4, 741.
- [57] M. Saliba, J.-P. Correa-Baena, C. M. Wolff, M. Stollerfoht, N. Phung, S. Albrecht, D. Neher, A. Abate, *Chem. Mater.* **2018**, 30, 4193.